Peer-reviewed version available at *Processes* **2020**, *8*, 946; doi:10.3390/pr8080946

Article

Magnetic Nanoparticles of Fe_3O_4 Biosynthesized by *Cnicus Benedictus* Extract: Photocatalytic Study of Organic Dye Degradation and Antibacterial Behavior

Álvaro de Jesús Ruíz-Baltazar [1]*, Simón Yobanny Reyes-López [2], Daniel Larrañaga-Ordáz[3], Nestor Méndez-Lozano[4], Marco Antonio Zamora Antuñano[4] and Ramiro Pérez[5]

[1] CONACYT-Centro de Física Aplicada y Tecnología Avanzada, Universidad Nacional Autónoma de México, Boulevard Juriquilla 3001, 76230 Santiago de Querétaro, QRO, México
[2] Instituto de Ciencias Biomédicas, Universidad Autónoma de Ciudad Juárez, Envolvente del PRONAF y Estocolmo s/n, Ciudad Juárez, CHIC., México, CP 32300
[3] Centro de Física Aplicada y Tecnología Avanzada, Universidad Nacional Autónoma de México, Boulevard Juriquilla 3001, 76230 Santiago de Querétaro, QRO, México
[4] Departamento de Ingeniería, Universidad del Valle de México, Campus Querétaro, Naranjos Punta Juriquilla 1000, Santa Rosa Jáuregui, Santiago de Querétaro, Qro. 76230, Mexico
[5] Instituto de Ciencias Físicas, Universidad Nacional Autónoma de México, Av Universidad s/n, Col. Chamilpa, Cuernavaca, MOR, 62210, México

* Corresponding autor: Álvaro de Jesús Ruíz-Baltazar; aruizbaltazar@fata.unam.mx; ORCID: 0000-0003-1032-3279

Abstract: Currently, the use of sustainable chemistry as an ecological alternative for the generation of products or processes, free of polluting substance has assumed a preponderant role. The aim of this work is propose a bioinspired, facile, at low cost, non-toxic and environmentally friendly alternative to obtaining magnetic nanoparticles whit a majority phase of magnetite (Fe_3O_4). Is important to empathize that the synthesis was based on the chemical reduction through the Cnicus Benedictus extract, whose use as reducing agent has not been reported in the synthesis of iron oxides nanoparticles. In addition, the Cnicus Benedictus is abundant endemic plant in Mexico, with several medicinal properties and a large number of natural antioxidants. The obtained nanoparticles exhibited significant magnetic and antibacterial properties and an enhanced photocatalytic activity. The crystallite size of the Fe_3O_4 nanoparticles (Fe_3O_4 NP's) was calculated by Williamson-Hall method. The photocatalytic properties of the Fe_3O_4 NP´s were studied by kinetics absorptions models in the Congo red (CR) degradation. Finally the antibacterial effect of the Fe3O4 NP´s were evaluated mediated the Kirby-Bauer method against E. coli and S. aureus bacteria. This route offers a green alternative to obtain Fe3O4 NP´s with remarkable magnetic, photocatalytic and antibacterial properties.

Keywords: Iron oxides; nanoparticles; organic dye degradation; photocatalytic effect antibacterial behavior

1. Introduction

In recent years, the development of the new nanomaterials and the nanoscience study has cobranded a preponderant place due to the wide number of researchers carried out in those fields. This is due to the notables physic, chemical, magnetic, optical, electronic and catalytic properties exhibits by the materials at the nanometric scale [1–3]. The quantic confinement of the atoms on the

Peer-reviewed version available at *Processes* **2020**, *8*, 946; doi:10.3390/pr8080946

nanoparticles favors the reactivity of the nanoparticles, given as results better properties associated with de nanoparticles in relationship to the bulk materials. Specifically, the Fe3O4 nanoparticles have been employed in several applications including magnetic resonance imaging (MRI), hyperthermia, drug delivery, heterogeneous catalysis, photocatalysis, magnetic carriers and wastewater treatment [4–10]. Some synthesis methodologies for obtaining Fe3O4 such as co-precipitations and thermal decomposition has been reported as the more common [11,12]. However, in many cases, the mentioned methods involve the use of surfactants, reducing agents and organic solvents which are toxic, expensive and whit a negative environmental impact[13–15]. In this sense, the new directrix for the synthesis of Fe3O4 nanoparticles is focused on the green chemical. Organic and biocompatibles molecules such as vitamin B12, glucose cellulose, amino acid and even plant extracts has been employed as stabilizing and/or reducing agents[16–20] . It is important to emphasize that the search for new alternatives that promote sustainable chemistry has become a priority issue. In this sense, endemic plants offer a sustainable and functional alternative to obtain nanomaterials [21–23]. On the other hand, it is well known that in recent years the use of plants as reducing agents (Myzus persicae, Ceratonia silique, Calotropis gigantean, Thymus kotschyanus leaf extract and pisumsativum peels) during the chemical synthesis of Fe3O4 nanoparticles has been widely reported [24–31]. However, the diversity of plants, properties and compounds present in each species is very wide and whose interaction in the synthesis process is reflected in the properties of the nanomaterials obtained. Therefore, it is important to study, propose and promote the use of endemic plants in nanomaterial synthesis processes. On the other hand, the applications of the Fe3O4 nanoparticles in the field of the degradation of organic pollutes and environmental remediation has been extensively studied due to their photocatalytic properties and the emerging needs for environmental remediation[32–35]. In this work, we reported an environmentally friendly alternative synthesis route of Fe3O4 nanoparticles with significant antibacterial and photocatalytic activity evaluated in Red Congo (CR) degradation. Kinetic absorption model was conducted to describe in detail the CR degradation process.

2. Materials and Methods

2.1. Bio-Synthesis of Fe3O4 nanoparticles

The synthesis of the particles was carried out from a precursor solution consisting of ferric chloride (FeCl3•6 H2O) and ferrous chloride (FeCl2•4H2O) in a 2: 1 molar ratio. The Fe+2 and Fe+3 ions were reduced using Cnicus Benedictus extract. Briefly, the Cnicus Benedictus extract was obtained drying and milled 3.87 g of Cnicus Benedictus leaves and mixing with 80 ml of deionized water. The mixture was heated to 150 °C for 15 min. After this time, the infusion obtained was filtered and transferred to the precursor solution of [Fe (III)/Fe (II)]. The pH of the mixture was adjusted to 12 by a NaOH solution. After 20 minutes of magnetically starring, the reduction of Fe ions was carried out. A color change of the post-reaction solution from dark reddish color into black color was observed. This coloration change suggests the formation of the Fe3O4 nanoparticles (Figure 1).

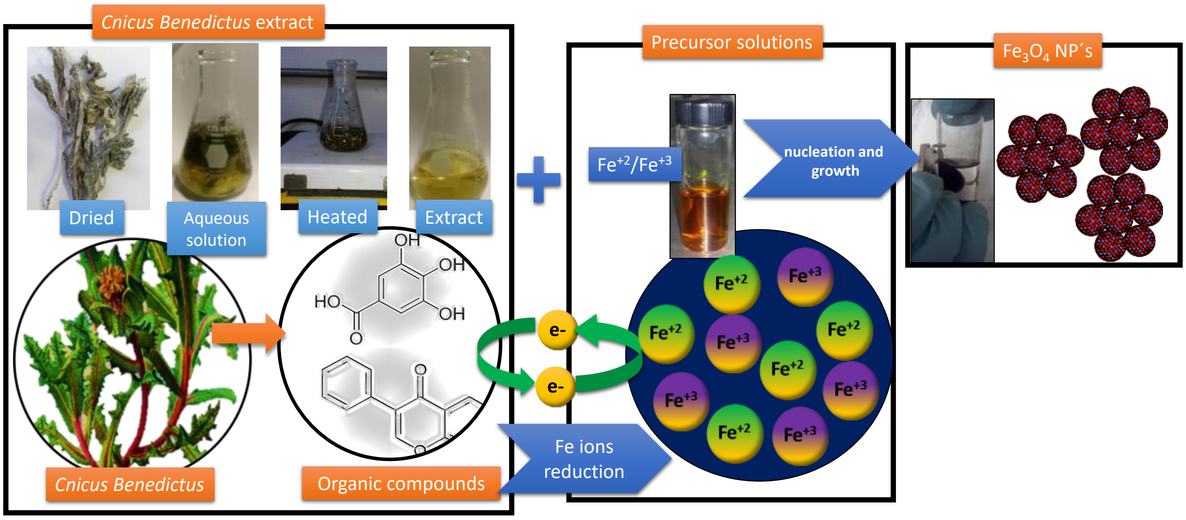

Figure 1. Schematic representation of the green procedure to obtaining Fe3O4 NP´s by Cnicus Benedictus as reducing agent

2.2 Congo red photo degradation

The photocatalytic activity assay of Fe3O4 nanoparticles was carried out through the degradation of CR. The experiments were performed using 1 ml of organic dye (CR) employed at 4 ppm. Posteriorly, Fe3O4 NP´s synthesized by Cnicus Benedictus were added to de CR solution. The concentration of Fe3O4 NP´s was 20 µg/ml. The CR photodegradation process was monitored by Uv-vis equipment in intervals of 3 min until the SPR of the CR disappeared.

2.3 Antibacterial activity.

The antibacterial effect was tested form the Kirby-Bauer method, The Gram-positive Staphylococcus aureus (S. aureus) and Gram-negative Escherichia coli (E. coli) bacteria were employed to determinate the antimicrobial behavior of the Fe3O4 NP´s. The microbial cultures were incubated at 36 °C for 24 h. Solutions of Fe3O4 NP´s were put in contact whit studied bacteria. Six filter papers paper discs of 5 mm of diameter were impregnated with 5 ml of Fe3O4 NP´s. Solutions of iron nanoparticles at different concentrations were performed and labeled. Specifically, C1 was associated with the disk control and the samples label as C2 (5mM), C3 (10 mM), C4 (15 mM), C5 (20 mM) and C6 (25 mM) correspond to the different Fe3O4 NP´s concentration. Finally, the measurements of the inhibition zone were collected. Statistically, an ANOVA analysis was employed to validate the measurement of the inhibition zone and consequently, the antibacterial effect of the Fe3O4 NP´s. The comparison between the antibacterial behavior of E. coli and S. aureus was modeled mathematically by curve fit models.

3. Results and Discussion

3.1. Scanning electron Microscopy.

The Fe3O4 NP´s were characterized by scanning electron microscopy (SEM), figure 2 (a) shows a secondary electrons image obtained at 15 kV, in this image is possible to identify the morphology and the distribution size of the Fe3O4 NP´s synthesized by Cnicus Benedictus. The Fe3O4 NP´s show agglomeration due to the steric effect of the nanoparticles [20]. However, in figure 2 (b), the individual nanoparticles confined in a cluster are observed. The average distribution size of the nanoparticles is

20 nm approximately. This value can be considered as a first approximation. Subsequent analysis by XRD can support this fact. Complementary, an EDS mapping of the sample is presented in figure 2 (c), which can be appreciated the Fe and O as constitutive elements of the sample. In this sense, is possible to affirm that the Fe3O4 NP´s can be synthesized by Cnicus Benedictus as reducing agent. Offering a new alternative in the green chemical in the field of synthesis of iron oxides nanoparticles Fe3O4 NP´s. Nevertheless, a more precise characterization of the iron oxides obtained is necessary and is presented below.

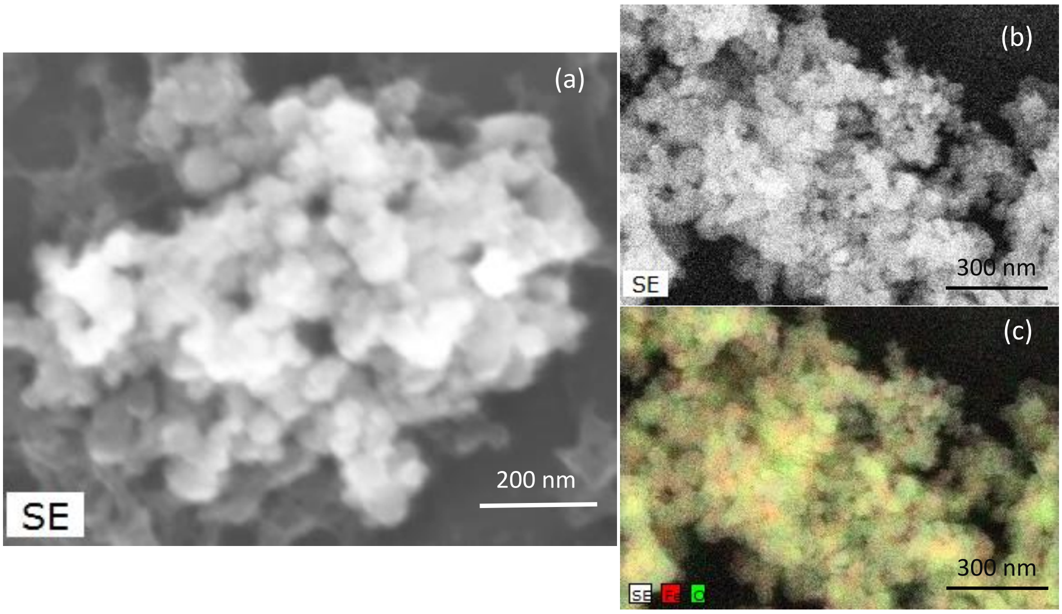

Figure 2. SEM image obtained by secondary electrons at (a) 130, (b) 80 kx and (c) EDS mapping of Fe3O4 NP´s obtained by *Cnicus Benedictus*.

3.1. X-Ray analysis of the nano-crystalline Fe3O4

Figure 3 (a) shows the experimental X-Ray diffraction pattern associated with the sample synthesized by the green route using Cnicus Benedictus. Based on the diffraction peaks observed in the experimental XRD pattern, it is possible to correlate this XRD pattern whit the cubic structure (Fm3m-325) of the magnetite (JCPDF# 96-900-5813). In order to support the structural characterization of the sample, Table 1, indicates the location of the diffraction peaks (2), interplanar distance (d-spacing) and the hkl index typical of the magnetite structure.

On the other hand, the crystallite size and strain can be calculated from the experimental XRD pattern according to the Williamson-Hall method. However, in the first part of the Williamson-Hall analysis, is necessary to obtaining parameters derivate to the fit of the peaks profile.

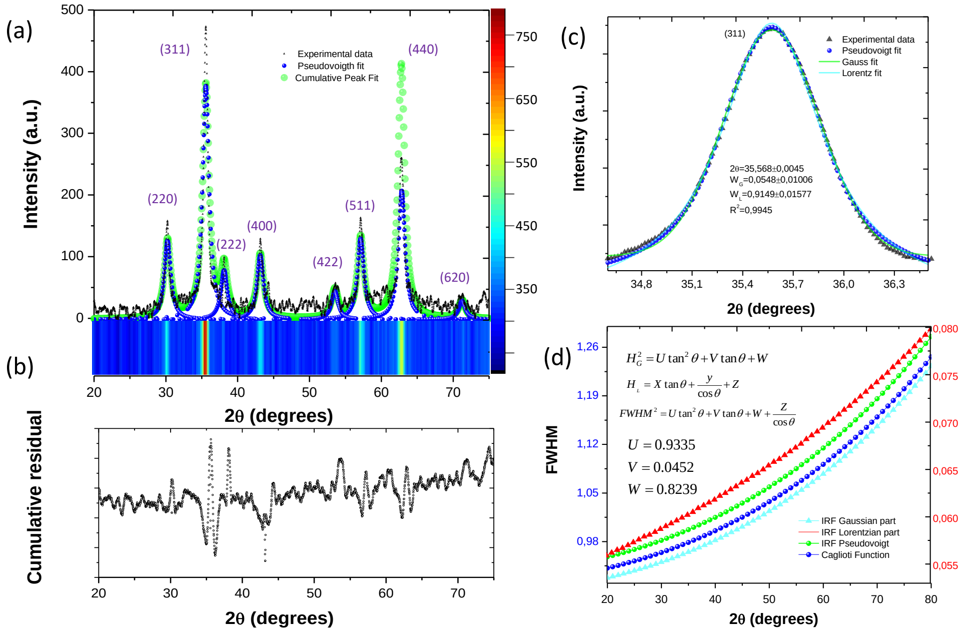

Figure 3. XRD pattern profile fitting and Pseudo-Voigt analysis of Broadening

The diffraction profile from the Fe3O4 nanoparticles was fitted with pseudo-Voigt (pV) function [38]. The pseudo-Voigt function is the convolution of Gauss and Lorentz functions. In general form, pV function is given by [39]:

$$pV(x) = \eta G(x) + (1-\eta)L(x) \qquad (1)$$

Where G(x) and L(x) are defined as the sum of the Gaussian peak and Lorentzian peak, respectively. In both functions, parameters such as Height (height of the peak at the maximum) peak center (position of the maximum) and FWHM (full width at half maximum of the peak) are involved. In this sense, is necessary to obtain the normalized peaks of Gauss (G´(x)) and Lorentz (L´(x)), consequently, the pV(x) can be expressed as

$$pV(x) = I[\eta G'(x,\Gamma) + (1-\eta)L'(x)] \qquad (2)$$

Where I is the intensity of the peak normalized by Gauss and Lorentz. Γ is the FWHM for the Gaussian and Lorentzian peaks, x_0 is the peak position and η is the Gaussian ratio. The Lorentzian part is described by

$$L'(x) = \frac{1}{\pi}\frac{\Gamma/2}{(x-x_{0)}{}^2 + (\Gamma/2)^2} \qquad (3)$$

And the Gaussian part is:

$$G'(x) = \frac{1}{\sigma\sqrt{2\pi}} e^{-\frac{(x-x_0)^2}{2\sigma^2}} \qquad (4)$$

Finally, the pseudo-Voigt expression employed for the fit profile peaks in the XRD analysis of the Fe3O4 nanoparticles, it can be written as follows[40]:

$$pV(x) = h * [\eta * \exp\left(-\frac{(x-x_0)^2}{-2\sigma^2}\right) + (1-\eta)\frac{(\Gamma/2)^2}{(x-x_{0)}{}^2 + (\Gamma/2)^2}] \qquad (5)$$

Where:

$$h = \frac{2I}{\pi\Gamma}\left[1 + \left(\sqrt{\pi ln2} - 1\right)\eta\right] \qquad (6)$$

$$\sigma = \frac{\Gamma}{2\sqrt{2ln2}} \qquad (7)$$

In this sense, figure 3 (a) and (b) show the multipeaks fitting analysis, and the cumulative residual fitting peak associated to the residual fit in the analysis, respectively.

Table 1. Parameters obtained from the XRD patterns of the Fe3O4 NP´s and involved in the Williamson-Hall analysis.

2θ	*d-spacing*	*hkl*	*FWHM (Corrected)*	*Asymmetry*	*Areal Asymmetry*	*Integral breadth*	*Shape factor*	*Size Uncorrected*	*Size Corrected*
30.24	2.9571	220	0.5069	1.0005	1.6403	0.588	0.861	18.03811703	18.3
35.62	2.5185	311	0.6984	0.7643	0.7378	0.893	0.782	13.27506532	13.4
38.1	2.4213	222	0.4058	0.6814	0.8878	0.242	1.68	23.01235689	24.1
43.2	2.0925	400	0.8135	1.4181	1.2442	0.277	2.936	11.67014924	11.8
53.62	1.7061	422	0.46792	1.1632	1.0717	0.3921	1.052	21.13618779	21.1
57.08	1.6102	511	0.7651	1.7009	1.1468	0.486	1.576	13.13289818	13.5
62.84	1.4802	440	0.6574	0.8412	0.994	0.646	1.017	15.73424925	16.6

In representative form about the fitting peaks, figure 2 (c) illustrate the fitting intensity associated to the (311) plane of the magnetite, in this plot is possible to observe the Gaussian and Lorentzian part corresponding to the Pseudo-Voigt fit process. In this case, a correlation factor (R2) of 0.9945 was observed. Consequently, this result indicates that the FWHM values are consistent for the subsequent analysis. In order to support the Pseudo-Voigt profile peak fitting, the instrumental resolution function (IRF) of the equipment was described in figure 3 (d). The IRF was plotted from the modified Caglioti equation, which is described follow [38]:

$$FWHM^2 = Utan^2\theta + V\tan\theta + W + \frac{Z}{\cos\theta} \qquad (7)$$

Complementary, the IRF was calculated by the Pseudo-voigt method. In this procedure, the Gaussian (HG) and the Lorentzian (HL) part were calculated started from the following expressions [39]:

$$H_G^2 = Utan^2\theta + V\tan\theta + W \qquad (8)$$

$$H_L = X\tan\theta + \frac{Y}{\cos\theta} + Z \qquad (9)$$

The HG and HL parts of the IRF were shown in graph 2(d). The convolution of the HG and HL is presented in the IRF PseudoVoigt (HpV) graph (figure 3 d). It is important to note that the HpV and the Caglioti curve are very similar due to the refinement of the U, V and W parameters.

3.2. *Williamson-Hall analysis*

Based on the results obtained from the Pseudo-Voigt analysis, the FWHM values were employed to calculate the crystallite size and strain, which can be obtained by the Williamson-Hall plot method. This method presupposes that the peaks observed from the X-Ray diffraction pattern are the convolution of the Gaussian part (broadening due to the strain) and the Lorentzian part (influence of the crystallite size) [6,39,41] Mathematically this relation can be expressed in the reciprocal space as:

$$\frac{\beta\cos\theta}{\lambda} = \frac{1}{D_V} + 2\varepsilon\left(\frac{2\sin\theta}{\lambda}\right) \qquad (10)$$

In this sense, from the graph of the $(\beta \cos\theta)$ versus $(2\sin\theta/\lambda)$ is possible to obtain the microstrain and domain size with the values of the slope and intercepts, respectively.

The Williamson-Hall plot is described in figure 4 (a). In this case, the crystallite size obtained by Pseudo-Voigt method is 17.47 nm. In order to corroborate this value, table 1 describes the parameter involved in the Williamson-Hall plot analysis. The profile function employed in the calculations was the Pseudo-Voigt model. However, the values of the Gauss and Lorentz parts were compared and showed in figure 4 (b) and (c), respectively. In all cases of the profile-fitting analysis of XRD peaks, similar values of crystallite size were obtained.

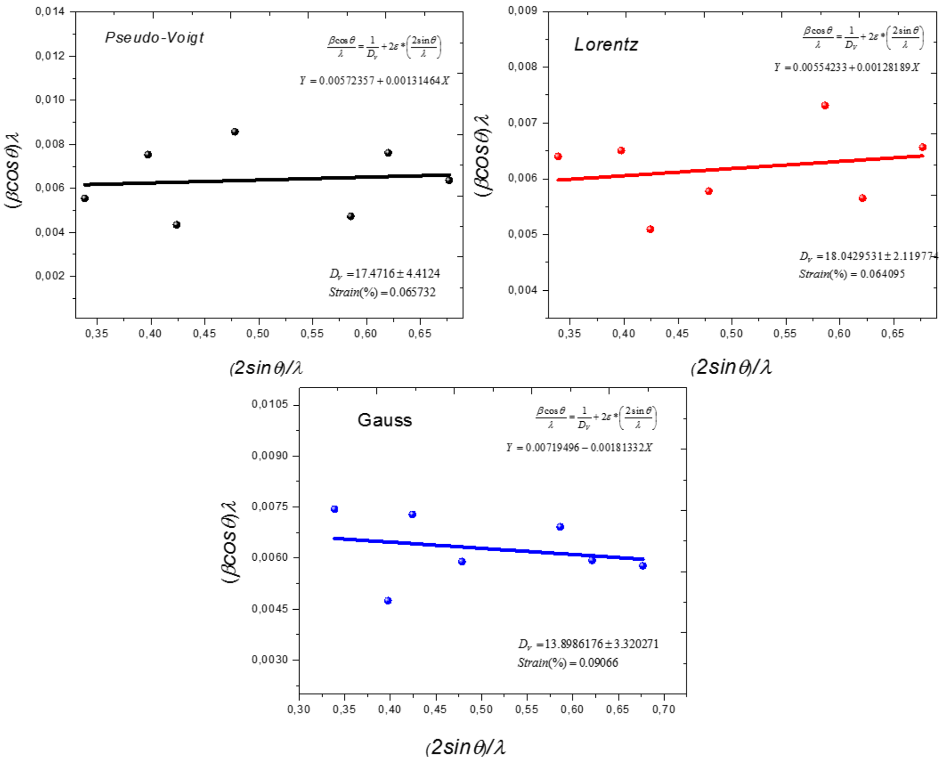

Figure 4. Williamson-Hall plot derivate from the XRD analysis of the Fe3O4 NP´s synthesized by Cnicus Benedictus

Table 2 shows the values of the crystallite size and strain calculated for the sample. The calculations performed based on the FWHM of each intensity, show a stable size and strain associated with the sample. In this case, the crystallite size is 14 nm according to the size observed by SEM. It is important to note that the Pseudo-Voigt method is a functional and highly accurate method for calculating the crystallite size from the XRD patterns due to this method it is a convolution of the Lorentz and Gauss method for fit peak profiles. Given as result an excellent tool for XRD pattern processing[38].

Table 2. Crystallite size and strain calculated from Pseudo-Voigt, Lorentz and Gauss methods.

Peer-reviewed version available at *Processes* **2020**, *8*, 946; doi:10.3390/pr8080946

Profile function	*Profile broadening*	*Size (nm)*	*Strain (%)*
Pseudo-Voigt	FWHM	17.47±4.41	0.065±0.014
	Integral breadth	18.10±4.32	0.1624±0.019
Lorentzian	FWHM	18.04±2.11	0.0640±0.017
	Integral breadth	22.11±4.98	0.032±0.016
Gaussian	FWHM	13.89±3.32	0.090±0.181
	Integral breadth	17.70±5.78	0.012±0.154

3.3. *Raman Spectroscopy*

In order to elucidate the oxidative phases obtained from the green synthesis of the nanoparticles, a Raman analysis is presented in figure 5. In this figure is possible identified three phases associated with the iron oxide. The main phase identified is magnetite whit an approximate of 45.5 %and the second d phase is the hematite (39.81 %) and the minority phase of maghemite (table 3). This result can be attributed to the facile oxidation of the NP´s due to the interaction with the medium. However, is important to mention that the XRD analysis supports the formation of Fe3O4 as main phase. However, the reduction of the Fe ions by Cnicus Benedictus was carried out, given as result the synthesis of Fe3O4. It has been reported that the presence of antioxidants in some organic extracts promotes Fe ions reduction[42]. Specifically, the Cnicus Benedictus extract offers a green alternative to obtain Fe3O4 NP´s.

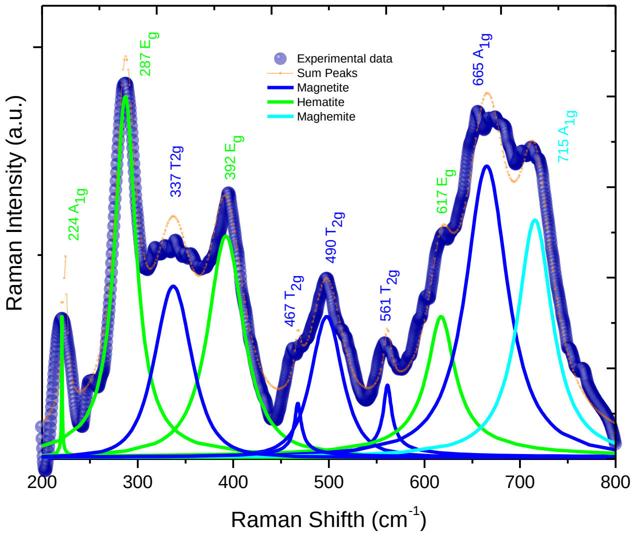

Figure 5. Deconvolution analysis of the Raman spectra of Fe3O4 NP´s.

Table 3 describes the location of the main intensities observed in the Raman spectra of the Fe3O4 NP´s synthesized by environmentally friendly methodology. Also, the phonon modes attributed to each intensity is showed in table 3. These values are supported by previous studies reported in the literature[43–45]. This result is conclusive respect to the iron oxide obtained by the green synthesis method although Cnicus Benedictus, in this sense we can affirm that is possible to obtain Fe3O4 NP´s y in majority phase and consequently evaluate the magnetic and catalytic properties of the magnetite.

Table 3. Deconvolution of Raman spectra for the quantification of iron oxide phases obtained by green synthesis route.

Peer-reviewed version available at Processes 2020, 8, 946; doi:10.3390/pr8080946

Phase	Center Max	Phonon modes	Max Height	FWHM	Area	% Phase
Magnetite	337.223	T_{2g}	205.855	454.371	1145.410	8.82417337
	467.565	T_{2g}	649.779	100.823	470.199	3.6223863
	490.854	T_{2g}	169.265	389.238	845.322	6.51231252
	561.327	T_{2g}	868.329	127.992	818.774	6.30778824
	665.161	A_{1g}	350.471	524.393	2627.970	20.2457311
						45.5123916
Hematite	224.171	A_{1g}	193.966	615.686	908.971	7.00266079
	287.060	E_g	434.132	275.124	1047.700	8.0714211
	392.236	E_g	266.167	444.447	1656.890	12.7645861
	617.429	E_g	169.405	38.060	1554.730	11.9775513
						39.8162194
Maghemite	715.584	A_{1g}	285.457	43.956	1904.400	**14.6713891**

3.4. Analysis of magnetic properties of the Fe3O4 obtained by green route.

Figure 6 shows the hysteresis curve or magnetization curve of the Fe3O4 NP´s. In this figure, we can observe an approximately superparamagnetic behavior [38,42,43] The saturation magnetization (Ms) value is 43.85 emu/g while the coercivity field (Hc) of the sample is 143.75 Oe. Both values are consistent whit the typical values reported in the literature for superparamagnetic materials[48,49]. In this sense is possible to affirm that the sample of Fe3O4 NP´s has effectively a superparamagnetic behavior and consequently, their potentials applications in optoelectronics or biomedicine among others, are notable. In other words, the green synthesis of Fe3O4 NP´s by Cnicus Benedictus offers an environmentally friendly alternative for magnetic nanoparticles obtaining.

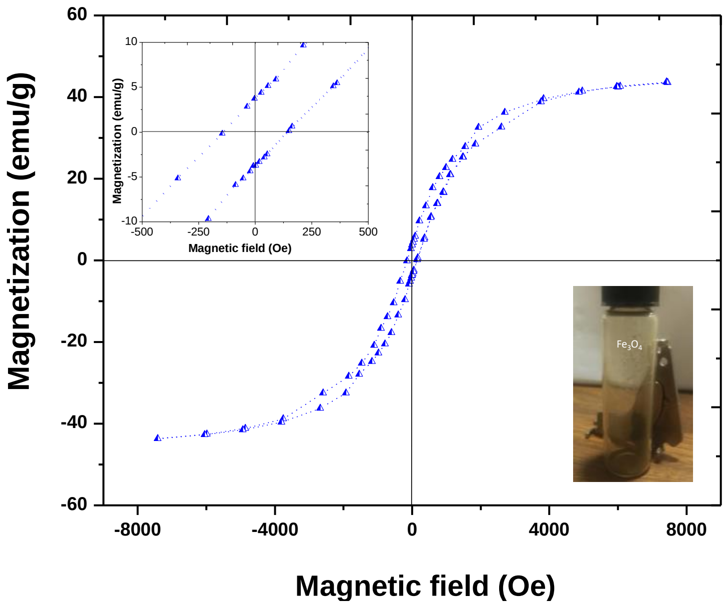

Figure 6. Magnetic hysteresis loop of the Fe3O4 NP´s at room temperature.

3.5. Photocatalytic effect: Congo red (CR) degradation

In order to evaluate the photocatalytic behavior of the Fe3O4 NP´s, a CR degradation process were conducted. Figure 7 (a) show the Uv-vis spectra associated to the CR, Fe3O4 NP´s and CR/ Fe3O4 samples at an initial time (t=0). In this figure, the characteristic peak associated to the CR is observed at 500 nm in the samples of CR and Fe3O4/CR. Figure 4 b illustrate the CR degradation process, in

Peer-reviewed version available at *Processes* **2020**, *8*, 946; doi:10.3390/pr8080946

which it is possible appreciates the CR degradation in a reaction time of 36 minutes. This fact indicates that the CR degradation by Fe3O4 NP´s is possible due to the reactivity of the nanoparticles obtained by green synthesis route.

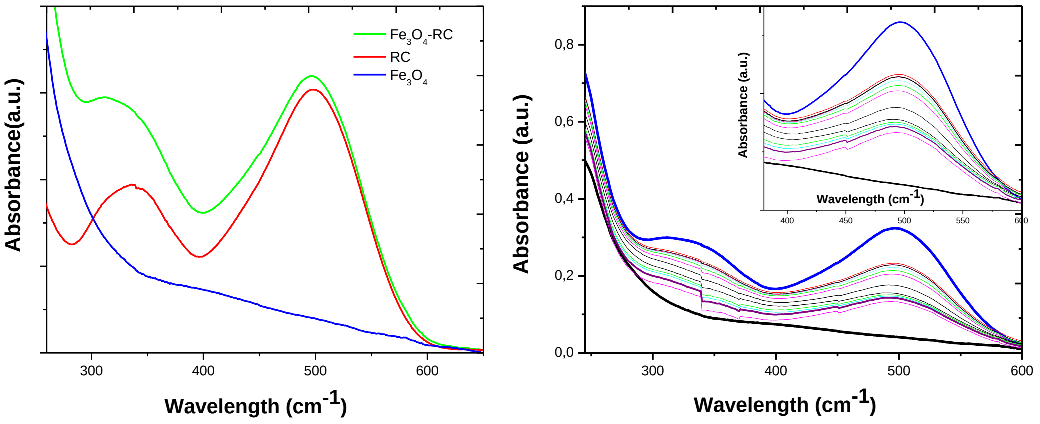

(a) (b)

Figure 7. (a) Uv-vis spectra of the (a) Fe3O4 NP´s, Fe3O4 NP´s-CR and CR (40 mgL-1) and (b) Congo red photodegradation by Fe3O4 NP´s synthesized using Cnicus Benedictus.

In general form, this behavior can be explained as combination of an oxidation and reduction process in which the surface of the Fe3O4 NP´s are a substrate where the CR molecules are absorbed. Subsequently, the nanoparticles act as actives sites for the electrons interactions between the organic dyes and Fe3O4 NP´s. The photocatalytic mechanism for organic dyes degradation involve the dye excitation under visible light with wavelength (λ> 400nm) from the ground state (Dye0) to the triplet excited state (Dye *). During this procedure, the excited state dye species generated semi-oxidized radial cation (Dye•+) by an electron injection into the conduction band of Fe3O4. Derivate to the reaction between the trapped electrons and the dissolved oxygen in the system, superoxide radical anions (O2 •−) are generated [50,51]. Consequently, this superoxide radicals anions give has result the hydroxyl radicals (OH•) formation [52–54], which are responsible to the oxidation and degradations of the organic dye compound presents in the CR (figure 8).

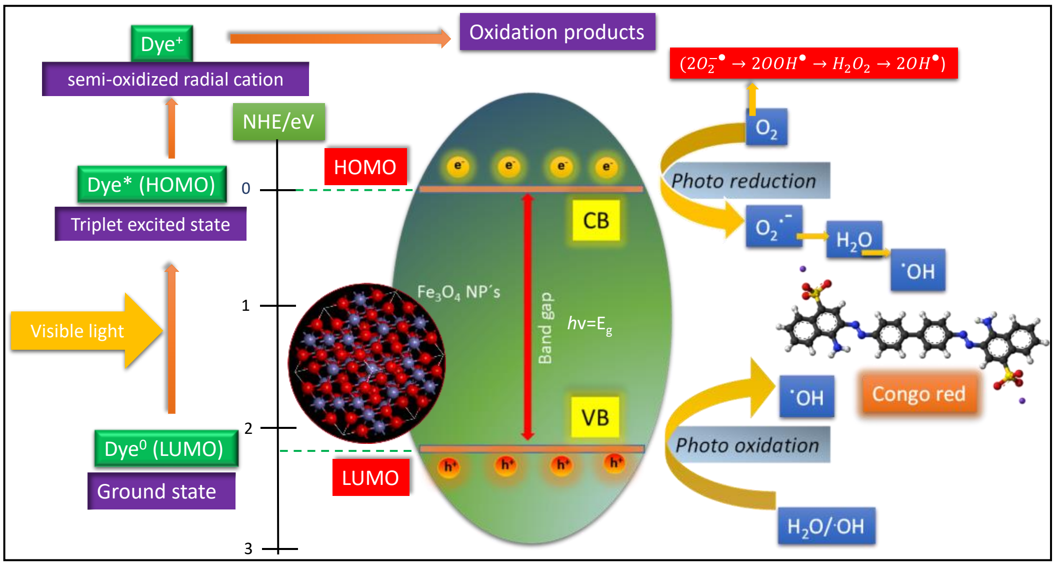

Figure 8. Schematic representation of dye photodegradation process

On the other hand, the adsorption rate and the equilibrium concentration at which the CR is degraded, can be described in detail by theoretical adsorption models.

3.6. *Theoretical adsorption kinetic models.*

In order to describe the adsorption kinetic behavior of the Fe3O4 NP´s, four theoretical models were analyzed with respect to the experimental data obtained from the photodegradation of the CR by Fe3O4 NP´s. Pseudo-firs order, Pseudo second order, Elovich and Intraparticle diffusion models were employed to describe and calculate the kinetics adsorption parameters of the organic dye. The equation that governs these model has been described on several reports[6,35,42,55].

Table 4. Theoretical adsorption models employed for the photodegradation of the CR by Fe3O4 NP´s

Theoretical model	Equation
Pseudo first order	$\frac{dq}{dt} = K_1(q_e - q_t)$ (11)
Pseudo second order	$\frac{dq}{dt} = K_2(q_e - q_t)^2$ (12)
Elovich	$\frac{dq_t}{dt} = \alpha e^{-\beta q_t}$ (13)
Intraparticle diffusion	$q_t = k_i\sqrt{t} + C_i$ (14)

Figure 9 a-d show the graphs associated to theoretical kinetic adsorption models. The correlation values existent between the experimental data and theoretical model are described in table 3. In this table is possible observe that the intraparticle diffusion model exhibits the highest correlation value R2, (0.9557). Based on this results, we can affirm that the CR degradation process is carried out although to the intraparticle diffusion process. From the physic-chemical point of view, the intraparticle diffusion model is described by tree steps. Firstly, an instantaneous adsorption is detected due that the concentration in the external solution is sufficiently high. In second place, a gradual adoption is observed during the CR degradation process. The time associated to this step depends to the some system variables such as temperature, absorbent particle size and solute concentration [56–59]. Finally, the organic molecules degraded exhibits a slow adsorption rate until the final equilibrium. Therefore, the intraparticle diffusion model can describe the CR degradation process and the solute concentration and the particle size of the Fe3O4 NP´s take a preponderant role in the CR degradation rate.

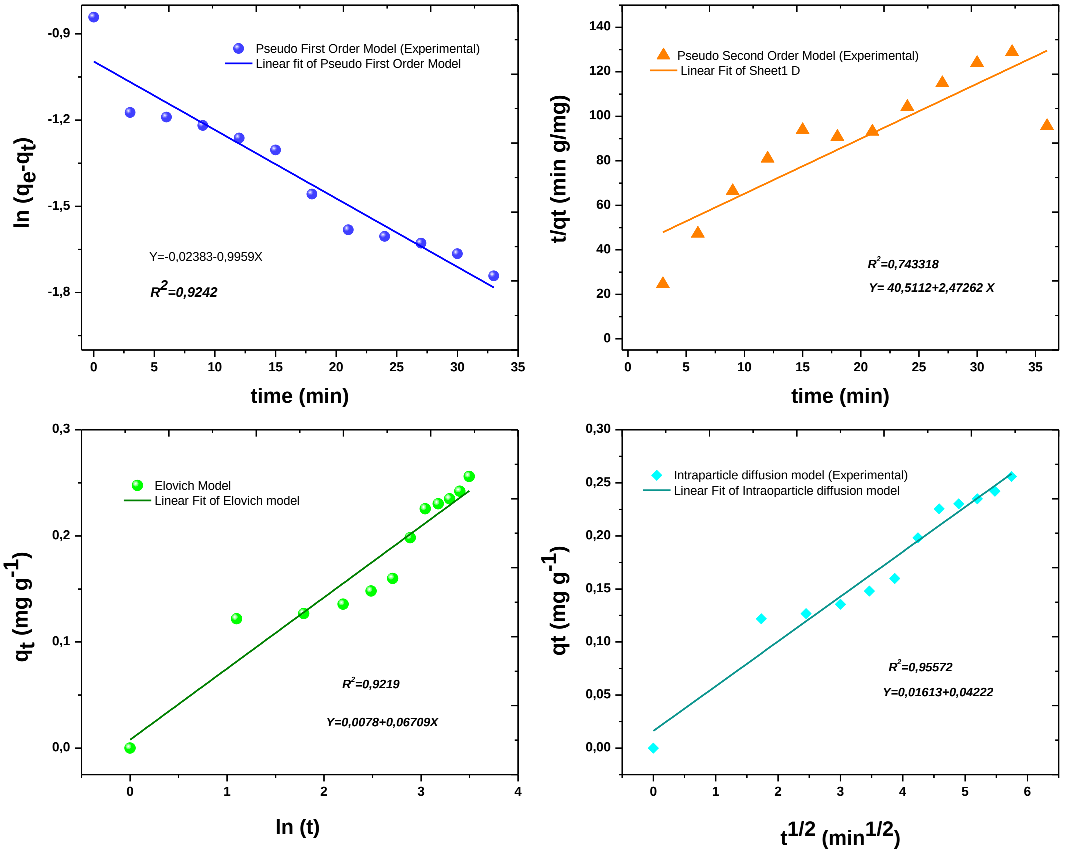

Figure 9. Experimental and theoretical kinetic adsorption models: (a) Pseudo first order, (b) Pseudo-second order, (c) Elovich and (d) Intraparticle diffusion models.

3.7. Antibacterial effect

In order to evaluate the antibacterial effect of the Fe3O4 NP´s obtained by green route, the inhibition zone in E. coli and S. aureus bacteria strains were measured. Figure 10 (a) display the inhibition zones presented by the Fe3O4 NP´s at Different Fe3O4 NP´s concentrations. In this plot, the antibacterial effect is mayor in the case of the E. Coli bacteria, in comparison of the S. aureus strain. Complementarily, the differences between the variances of inhibition zone were determinates by an ANOVA analysis. In this process, the p-value corresponding to the F-statistic is lower than 0.05 ($p< 0.05$), this value suggesting that the one or more treatments are significantly different. Derivate to this result, is possible to affirm, that the Fe3O4 NP´s obtained by Cnicus Bendictus have an antibacterial effect due to the box-plot of the ANOVA analysis (figure 10 b) show a significant differences in relation to the control sample. In this case, C1 is associated to the disk control and the samples label as C2 (5mM), C3 (10 mM), C4 (15 mM), C5 (20 mM) and C6 (25 mM) correspond to the Fe3O4 NP´s concentration. On the other hand, post hoc Tukey HSD test can be employed to identify which pairs of treatments are significantly different from each other. Figure 10 (c) illustrate graphically the Tukey test and the pair of the treatments with significant differences (inset figure 10 c). Through these results, the bactericidal effect of nanoparticles can be statistically corroborated. It has been verified that this effect is related to the capacity of the particles to interact with the bacterial membrane, generating structural and physiological changes in the microorganism, generating its elimination. It is has been reported that the Fe3O4 NP´s exhibits remarkable reactivity with phosphorus and sulfur compounds which are presents in the proteins of the cell membrane in the bacteria[60,61]. On the other hand, the generation extracellular reactive oxygen species (ROS) by oxidation Fe3O4 NP´s has been associated to the antibacterial mechanism of Fe3O4 NP´s[62] . In this sense, the difference between the antibacterial effect presented by the E. coli and S. aureus can be attributed to the structural differences associated to the gram positive and gram negative bacteria and their cell membranes. In the case of the gram positive bacteria (S. Aureus), the cell membrane is smooth and single-layered and the thickness of the cell wall is 20 to 80 nanometers, while in the case of the gram negative bacteria (E. Coli), have a wavy and double-layered cell-wall, but the thickness of the cell wall is significant minor un comparison with the gram positive bacteria. In this sense, the major antibacterial effect observed in the E. coli bacteria can be explained as function of their cellular structure and cell wall morphology[25].

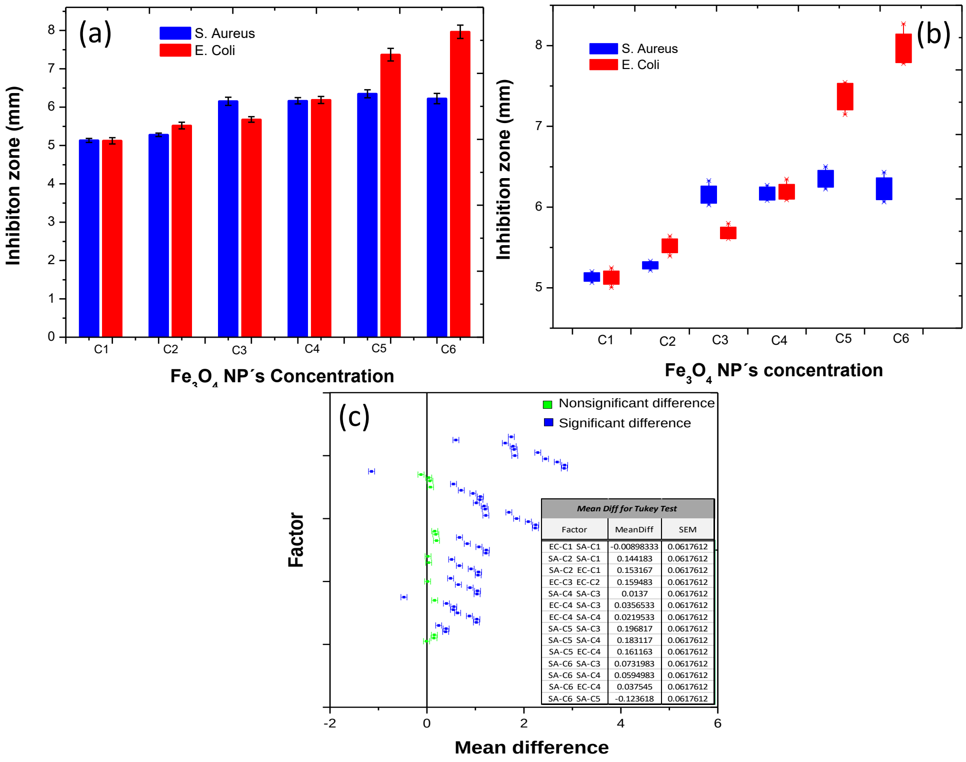

Mean Diff for Tukey Test		
Factor	MeanDiff	SEM
EC-C1 SA-C1	-0.00898333	0.0617612
SA-C2 SA-C1	0.144183	0.0617612
SA-C2 EC-C1	0.153167	0.0617612
EC-C3 EC-C2	0.159483	0.0617612
SA-C4 SA-C3	0.0137	0.0617612
EC-C4 SA-C3	0.0356533	0.0617612
EC-C4 SA-C4	0.0219533	0.0617612
SA-C5 SA-C3	0.196817	0.0617612
SA-C5 SA-C4	0.183117	0.0617612
SA-C5 EC-C4	0.161163	0.0617612
SA-C6 SA-C3	0.0731983	0.0617612
SA-C6 SA-C4	0.0594983	0.0617612
SA-C6 EC-C4	0.037545	0.0617612
SA-C6 SA-C5	-0.123618	0.0617612

Figure 10. (a) Bar graphs of the diameter of the inhibition zone measured from the bacterial susceptibility, (b) Box-plot of antibacterial activity of Fe3O4 against S. aureus and E. coli bacteria. (b) Scatter plot of Tukey comparison by pairs

Peer-reviewed version available at Processes 2020, 8, 946; doi:10.3390/pr8080946

Finally, and based on the experimental data corresponding to antibacterial behavior of the Fe3O4 NP´s, it is can be modelling mathematically. Starting to the graph 11 (a) which describe the antibacterial response of the E. Coli and S. Aureus bacteria to the Fe3O4 NP´s , it is possible associated this behavior to the sigmoid dose-response curve model fit, which is described by the follow equation:

$$y = A_1 + \frac{A_1 - A_2}{1+10^{(logx_0 - x)p}} \qquad (15)$$

Figure 11 (b) modelling graphically the antibacterial response of the S. aureus bacteria to the Fe3O4 NP´s synthesized by Cnicus Benedictus and their corresponding parameter. It is important to note that the correlation factor R2 is 0.98, Thus, the dose response fitting can be describe whit high precision the experimental bactericidal behavior of the S. aureus.

On the other hand, the bactericidal effect of the Fe3O4 NP´s against E. coli, also was modelling mathematically. However, the best-fit of the experimental data associated to de gram negative bacteria (E. coli) were fit to the two sites competition model, which is described by:

$$y = A_2 + \frac{A_1 - A_2}{1+10^{(x - logx_{01})}} + \frac{A_1 - A_2(1-f)}{1+10^{(x - logx_{02})}} \qquad (16)$$

In this case, the R2 value were 0.998 and their associated parameter are inset in the figure 11 (c). Consequently, by the two sites competition model can be describe the bactericidal behavior of the Fe3O4 NP´s against E. coli bacteria. This fact indicate that the two site competition model attributed to the antibacterial effect against E. coli is more complex in comparison to the S. aureus behavior. However, this effect is notable mayor. This fact support the discussion referent to the characteristics of the gram positive and gram negative bacteria described anteriorly. Due that the thickness of the cell wall of the bacteria, has a preponderant paper in the antibacterial behavior.

Peer-reviewed version available at *Processes* **2020**, *8*, 946; doi:10.3390/pr8080946

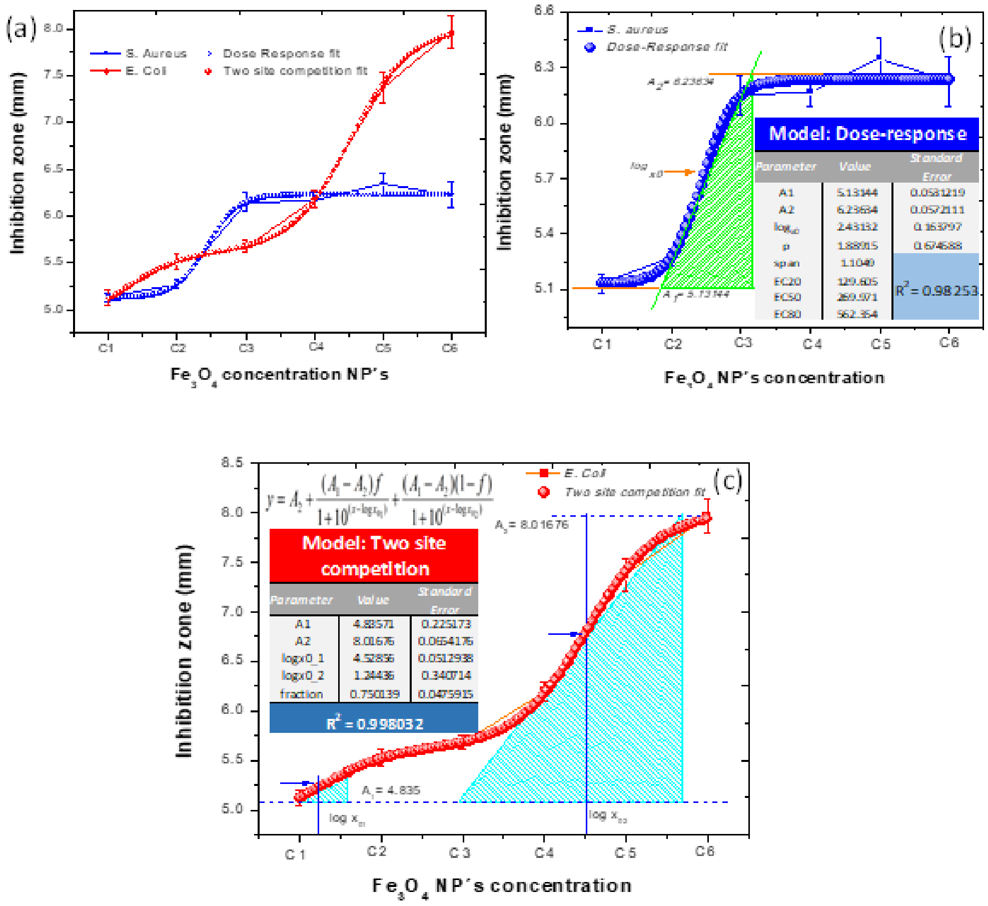

Model: Dose-response

Parameter	Value	Standard Error
A1	5.13144	0.0581219
A2	6.23634	0.0572111
$\log x_0$	2.43132	0.163797
p	1.88015	0.674688
span	1.1049	$R^2 = 0.98253$
EC20	129.605	
EC50	269.971	
EC80	562.354	

$$y = A_2 + \frac{(A_1 - A_2)f}{1+10^{(x-\log x_{01})}} + \frac{(A_1 - A_2)(1-f)}{1+10^{(x-\log x_{02})}}$$

Model: Two site competition

Parameter	Value	Standard Error
A1	4.83571	0.225173
A2	8.01676	0.0654176
logx0_1	4.52836	0.0512938
logx0_2	1.24436	0.340714
fraction	0.750139	0.0475915

$R^2 = 0.998032$

Figure 11. Antibacterial curve fitting (a) comparison between E. coli and S. aureus (b) S. aureus behavior (Dose response model), and (c) E. Coli behavior (two sites competition model)

In conclusive form, is possible to affirm that the gram negative bacteria (s. aureus) is more susceptible to the interaction with the Fe3O4 NP's which exhibits high specific surface area, promoting a better contact with the microorganisms, and consequently, the Fe3O4 NP's can be attached to the cell membrane and penetrate inside the bacteria.

4. Conclusions

The green synthesis by Cnicus Benedictus as reducing agent offer an environmental friendly alternative to obtaining Fe3O4 NP´s. the organic compound presents in the Cnicus Benedictus extract have the capacity to carried out the iron ions reduction and consequently, the Fe3O4 NP´s formation in majority phase. Iron oxides such as hematite and maghemite were also observed. However, the mentioned iron oxide appears in minor phase due to the great reactivity of the iron oxides with the aqueous media promoting the facile oxidation of the iron oxide species. On the other hand, the obtained Fe3O4 NP´s, show a very similar behavior to the superparamagnetic materials. This fact, indicates that the nanoparticles synthesized can be evaluated for potential application in the magnetism materials fields among other. Additionally, this research was focused in environmental remediation applications, specifically in the Congo red photodegradation. Conclusively, it was observed that the Fe3O4 NP´s are capable of carrying out the photodegradation of the organic dye (CR). Finally is possible to affirm that the Fe3O4 NP´s synthesized by green route, offer a facile, at low cost, non-toxic and environmental friendly alternative to obtaining functional Fe3O4 NP´s with proved magnetic and catalytic properties. Also, is possible to affirm that the Fe3O4 NP´s exhibit an antibacterial effect. However, the gram negative bacteria (s. aureus) is more susceptible to the interaction with the Fe3O4 NP´s which exhibits high specific surface area, promoting a better contact with the microorganisms, and consequently, the Fe3O4 NP´s can be attached to the cell membrane and penetrate inside the bacteria.

Author Contributions: Conceptualization, formal analysis, investigation, writing—original draft preparation and project administration, Álvaro de Jesús Ruíz-Baltazar; Investigation and review and editing, Simón Yobanny Reyes-López; methodology, Daniel Larrañaga-Ordaz; investigation, data curation, N. Méndez-Lozano; investigation, review and editing, M.A. Zamora Antuñano; R. Pérez, review and editing. All authors have read and agreed to the published version of the manuscript

Acknowledgments: Álvaro de Jesús Ruíz-Baltazar appreciates the support provided by the National Council for Science and Technology (CONACYT, México) in collaboration with the Center of Applied Physics and Advanced Technology (CFATA-UNAM) through "Cathedra CONACYT" program. Likewise, to the national materials characterization laboratory (LaNCaM) belonging to CFATA-UNAM.

Conflicts of Interest: The authors declare no conflict of interest for the publication of this work.

References

1. Ahmed, M. a.; Abou-Gamra, Z.M.; ALshakhanbeh, M. a.; Medien, H. Control synthesis of metallic gold nanoparticles homogeneously distributed on hexagonal ZnO nanoparticles for photocatalytic degradation of methylene blue dye. *Environ. Nanotechnology, Monit. Manag.* **2019**, *12*, 100217, doi:10.1016/j.enmm.2019.100217.

2. Patwardhan, S. V.; Manning, J.R.H.; Chiacchia, M. Bioinspired synthesis as a potential green method for the preparation of nanomaterials: Opportunities and challenges. *Curr. Opin. Green Sustain. Chem.* **2018**, *12*, 110–116, doi:10.1016/j.cogsc.2018.08.004.

3. Carabineiro, S.A.C. Supported Gold Nanoparticles as Catalysts for the Oxidation of Alcohols and Alkanes. **2019**, *7*, doi:10.3389/fchem.2019.00702.

4. Reactors, M. Photocatalytic Membranes in Photocatalytic Membrane Reactors. **2018**, doi:10.3390/pr6090162.

5. Meramo-hurtado, S.I.; Zuorro, A. applied sciences Environmental Assessment of Large Scale Production of Magnetite (Fe 3 O 4) Nanoparticles via Coprecipitation.

6. Abatement, E.; Cationic, A.; Jain, B.; Hashmi, A.; Sanwaria, S.; Singh, A.K. Catalytic Properties of Graphene Oxide Synthesized by a " Green " Process for Catalytic Properties of Graphene Oxide Synthesized by a " Green " Process for Efficient Abatement of Auramine-O Cationic Dye. **2020**, doi:10.1080/22297928.2020.1747536.

7. Aghazadeh, M.; Karimzadeh, I.; Ganjali, M.R.; Mohebi Morad, M. A novel preparation method for surface coated superparamagnetic Fe3O4 nanoparticles with vitamin C and sucrose. *Mater. Lett.* **2017**, *196*, 392–395, doi:10.1016/j.matlet.2017.03.064.

8. Zhang, H.; Zhao, J.; Ou, X. Facile synthesis of Fe3O4 nanowires at low temperature (80 °C) without autoclaves and their electromagnetic performance. *Mater. Lett.* **2017**, *209*, 48–51, doi:10.1016/j.matlet.2017.07.071.

9. Hoseinpour, V.; Ghaemi, N. Green synthesis of manganese nanoparticles: Applications and future

perspective–A review. *J. Photochem. Photobiol. B Biol.* **2018**, *189*, 234–243, doi:10.1016/j.jphotobiol.2018.10.022.

10. S, M. Halide removal from water using silver doped magnetic-microparticles. **2020**, *253*, doi:10.1016/j.jenvman.2019.109731.

11. Mi, S.; Liu, R.; Li, Y.; Xie, Y.; Chen, Z. Large low-field magnetoresistance of Fe3O4 nanocrystal at room temperature. *J. Magn. Magn. Mater.* **2017**, *428*, 235–238, doi:10.1016/j.jmmm.2016.12.071.

12. Xu, J.; Li, Q.; Zong, W.; Zhang, Y.; Li, S. Ultra-wide detectable concentration range of GMR biosensors using Fe3O4 microspheres. *J. Magn. Magn. Mater.* **2016**, *417*, 25–29, doi:10.1016/j.jmmm.2016.05.059.

13. Andr, L.; Hernandez-ramirez, A.; Machuca-martinez, F. Recent Developments in the Photocatalytic Treatment of Cyanide Wastewater : An Approach to Remediation.

14. Aguas, Y.; Hincapi, M.; Camilo, S.; Botero, L.; Fern, P. Photocatalytic Inactivation of Enterobacter cloacae and Escherichia coli Using Titanium Dioxide Supported on Two Substrates. **2018**, doi:10.3390/pr6090137.

15. Agueda, V.I.; Larriba, M.; Delgado, J.A. Enhanced removal of the endocrine disruptor compound Bisphenol A by adsorption onto green-carbon materials . Effect of real effluents on the adsorption process. **2020**, *266*, doi:10.1016/j.jenvman.2020.110604.

16. David, L.; Moldovan, B. Green Synthesis of Biogenic Silver Nanoparticles for E ffi cient Catalytic Removal of Harmful Organic Dyes. **2020**.

17. Ali, E.M. E ff ective Inhibition of Candidiasis Using an Eco-Friendly Leaf Extract of Calotropis - gigantean -Mediated Silver Nanoparticles. **2020**, 1–16.

18. Sharifi-rad, M.; Pohl, P. Synthesis of Biogenic Silver Nanoparticles (AgCl-NPs) Using a Pulicaria vulgaris Gaertn . Aerial Part Extract and Their Application as Antibacterial , Antifungal and Antioxidant Agents. **2020**.

19. Costale, A.; Cravotto, G. Plant and Biomass Extraction and Valorisation under Hydrodynamic Cavitation. **2019**, 1–19.

20. Ribeiro, R.P.P.L.; Barreto, J.; Xavier, M.D.G.; Martins, D.; Esteves, A.A.C.; Branco, M.; Tirolien, T.; Mota, J.P.B.; Bonfait, G. Cryogenic Neon Adsorption on Co3(ndc)3(dabco) Metal-Organic Framework. *Microporous Mesoporous Mater.* **2020**, *3*, 110055, doi:10.1016/j.micromeso.2020.110055.

21. Gene, M. Enhanced Silver Nanoparticle Synthesis by Escherichia Coli Transformed with Candida Albicans. **2019**.

22. Catalysis, R.; Yu, C.; Tang, J.; Liu, X.; Ren, X.; Zhen, M. Green Biosynthesis of Silver Nanoparticles Using Eriobotrya japonica (Thunb .) Leaf Extract for. **2019**, doi:10.3390/ma12010189.

23. Lorenzo, J.M.; Barba, F.J. Green Chemistry. **2020**, 2325–2353, doi:10.1039/c9gc03878g.

24. Fakhri, A.; Tahami, S.; Nejad, P.A. Preparation and characterization of Fe3O4-Ag2O quantum dots decorated cellulose nanofibers as a carrier of anticancer drugs for skin cancer. *J. Photochem. Photobiol. B Biol.* **2017**, *175*, 83–88, doi:10.1016/j.jphotobiol.2017.08.032.

25. Naeimi, H.; Nazifi, Z.S.; Amininezhad, S.M. Preparation of Fe3O4 encapsulated-silica sulfonic acid nanoparticles and study of their in vitro antimicrobial activity. *J. Photochem. Photobiol. B Biol.* **2015**, *149*, 180–188, doi:10.1016/j.jphotobiol.2015.06.004.

26. Marimón-Bolívar, W.; González, E.E. Green synthesis with enhanced magnetization and life cycle assessment of Fe3O4 nanoparticles. *Environ. Nanotechnology, Monit. Manag.* **2018**, *9*, 58–66, doi:10.1016/j.enmm.2017.12.003.

27. Prasad, C.; Krishna Murthy, P.; Hari Krishna, R.H.; Sreenivasa Rao, R.; Suneetha, V.; Venkateswarlu, P. Bio-inspired green synthesis of RGO/Fe3O4 magnetic nanoparticles using Murrayakoenigii leaves extract and its application for removal of Pb(II) from aqueous solution. *J. Environ. Chem. Eng.* **2017**, *5*, 4374–4380, doi:10.1016/j.jece.2017.07.026.

28. Beyene, H.D.; Werkneh, A.A.; Bezabh, H.K.; Ambaye, T.G. Synthesis paradigm and applications of silver nanoparticles (AgNPs), a review. *Sustain. Mater. Technol.* **2017**, *13*, 18–23, doi:10.1016/j.susmat.2017.08.001.

29. Li, W.H.; Yang, N. Green and facile synthesis of Ag-Fe3O4 nanocomposites using the aqueous extract of Crataegus pinnatifida leaves and their antibacterial performance. *Mater. Lett.* **2016**, *162*, 157–160, doi:10.1016/j.matlet.2015.09.064.

30. Patra, J.K.; Baek, K.H. Green biosynthesis of magnetic iron oxide (Fe3O4) nanoparticles using the aqueous extracts of food processing wastes under photo-catalyzed condition and investigation of their antimicrobial and antioxidant activity. *J. Photochem. Photobiol. B Biol.* **2017**, *173*, 291–300, doi:10.1016/j.jphotobiol.2017.05.045.

31. Dominguez, J.R.; Gonzalez, T.; Cuerda-correa, E.M.; Muñoz-peña, M.J. Combating paraben pollution in surface waters with a variety of photocatalyzed systems : Looking for the most efficient technology. **2019**, 1317–1327.

32. Gonz, T.; Dominguez, J.R.; Cuerda-correa, E.M.; Correia, S.E.; Donoso, G. Selecting and improving activated homogeneous catalytic processes for pollutant removal . Kinetics , mineralization and optimization. **2020**, *256*, doi:10.1016/j.jenvman.2019.109972.

33. Perales, M.F.; Rozalen, M.; Polo, M.S.; Utrilla, J.R. Solar Degradation of Sulfamethazine Using rGO / Bi Composite Photocatalysts Solar Degradation of Sulfamethazine Using rGO / Bi Composite Photocatalysts. **2020**, doi:10.3390/catal10050573.

34. Moreno-castilla, C. Removal of Phenolic Compounds from Water Using Copper Ferrite Nanosphere Composites as Fenton Catalysts. **2019**.

35. Peluso, A.; Gargiulo, N.; Aprea, P.; Pepe, F.; Peluso, A.; Gargiulo, N.; Aprea, P.; Pepe, F.; Peluso, A.;

Gargiulo, N.; et al. Nanoporous Materials as H 2 S Adsorbents for Biogas Purification : a Review Nanoporous Materials as H 2 S Adsorbents for Biogas Puri fi cation : a Review. *Sep. Purif. Rev.* **2018**, *00*, 1–12, doi:10.1080/15422119.2018.1476978.

36. Tabatabai Yazdi, S.; Iranmanesh, P.; Saeednia, S.; Mehran, M. Structural, optical and magnetic properties of MnxFe3−xO4 nanoferrites synthesized by a simple capping agent-free coprecipitation route. *Mater. Sci. Eng. B Solid-State Mater. Adv. Technol.* **2019**, *245*, 55–62, doi:10.1016/j.mseb.2019.05.009.

37. Andrzejewski, B.; Bednarski, W.; Kaźmierczak, M.; Łapiński, A.; Pogorzelec-Glaser, K.; Hilczer, B.; Jurga, S.; Nowaczyk, G.; Załęski, K.; Matczak, M.; et al. Magnetization enhancement in magnetite nanoparticles capped with alginic acid. *Compos. Part B Eng.* **2014**, *64*, 147–154, doi:10.1016/j.compositesb.2014.04.022.

38. Scardi, P.; Ermrich, M.; Fitch, a.; Huang, E.W.; Jardin, R.; Kuzel, R.; Leineweber, a.; Mendoza Cuevas, a.; Misture, S.T.; Rebuffi, L.; et al. Size–strain separation in diffraction line profile analysis. *J. Appl. Crystallogr.* **2018**, *51*, 831–843, doi:10.1107/S1600576718005411.

39. Sen, R.; Das, G.C.; Mukherjee, S. X-ray diffraction line profile analysis of nano-sized cobalt in silica matrix synthesized by sol-gel method. *J. Alloys Compd.* **2010**, *490*, 515–523, doi:10.1016/j.jallcom.2009.10.072.

40. Mittal, M.; Gupta, A.; Pandey, O.P. Role of oxygen vacancies in Ag/Au doped CeO 2 nanoparticles for fast photocatalysis. *Sol. Energy* **2018**, *165*, 206–216, doi:10.1016/j.solener.2018.03.033.

41. Asthana, A.; Chakraborty, R.; Jain, B.; Singh, A.K.; Switching, E. Cationic Dye Removal Using Novel Magnetic / Activated Charcoal / β -Cyclodextrin / Alginate Polymer Nanocomposite. **2020**, doi:10.3390/nano10010170.

42. Ruíz-Baltazar, Á.D.J. Green Composite Based on Silver Nanoparticles Supported on Diatomaceous Earth: Kinetic Adsorption Models and Antibacterial Effect. *J. Clust. Sci.* **2018**, doi:10.1007/s10876-018-1357-7.

43. Shebanova, O.N.; Lazor, P. Raman spectroscopic study of magnetite (FeFe2O4): A new assignment for the vibrational spectrum. *J. Solid State Chem.* **2003**, *174*, 424–430, doi:10.1016/S0022-4596(03)00294-9.

44. Jubb, A.M.; Allen, H.C. Vibrational spectroscopic characterization of hematite, maghemite, and magnetite thin films produced by vapor deposition. *ACS Appl. Mater. Interfaces* **2010**, *2*, 2804–2812, doi:10.1021/am1004943.

45. Rothen-rutishauser, B.; Petri-fink, A. Characterization of the Shape Anisotropy of Superparamagnetic Iron Oxide Nanoparticles during Thermal Decomposition. **2020**.

46. Huaccallo, Y.; Álvarez-torrellas, S.; Marín, M.P.; Gil, M.V.; Larriba, M.; Águeda, V.I.; Ovejero, G.; García, J. Magnetic Fe 3 O 4 / multi-walled carbon nanotubes materials for a highly efficient depletion of diclofenac by catalytic wet peroxideoxidation. **2019**, 22372–22388.

47. Hekmatara, H.; Seifi, M.; Forooraghi, K. Microwave absorption property of aligned MWCNT/Fe3O4. *J. Magn. Magn. Mater.* **2013**, *346*, 186–191, doi:10.1016/j.jmmm.2013.06.032.

48. Zhou, X.; Shi, Y.; Ren, L.; Bao, S.; Han, Y.; Wu, S.; Zhang, H.; Zhong, L.; Zhang, Q. Controllable synthesis, magnetic and biocompatible properties of Fe 3 O 4 and α-Fe 2 O 3 nanocrystals. *J. Solid State Chem.* **2012**, *196*, 138–144, doi:10.1016/j.jssc.2012.05.025.

49. Qin, Y.; Zhang, H.; Tong, Z.; Song, Z.; Chen, N. A facile synthesis of Fe3O4@SiO2@ZnO with superior photocatalytic performance of 4-nitrophenol. *J. Environ. Chem. Eng.* **2017**, *5*, 2207–2213, doi:10.1016/j.jece.2017.04.036.

50. Ajmal, A.; Majeed, I.; Malik, R.N.; Idriss, H.; Nadeem, M.A. Principles and mechanisms of photocatalytic dye degradation on TiO 2 based photocatalysts: A comparative overview. *RSC Adv.* **2014**, *4*, 37003–37026, doi:10.1039/c4ra06658h.

51. Singh, A.K. Assessing the Photocatalytic Degradation of Fluoroquinolone Norfloxacin by Mn : ZnS Quantum Dots : Kinetic Study , Degradation Pathway and Influencing Assessing the Photocatalytic Degradation of Fluoroquinolone Norfloxacin by Mn : ZnS Quantum Dots : Kinetic Study , Degradation Pathway and Influencing Factors. **2020**, doi:10.3390/nano10050964.

52. Wang, N.; Zheng, T.; Zhang, G.; Wang, P. A review on Fenton-like processes for organic wastewater treatment. *J. Environ. Chem. Eng.* **2016**, *4*, 762–787, doi:10.1016/j.jece.2015.12.016.

53. Zazouli, M.A.; Ghanbari, F.; Yousefi, M.; Madihi-Bidgoli, S. Photocatalytic degradation of food dye by Fe3O4-TiO2 nanoparticles in presence of peroxymonosulfate: The effect of UV sources. *J. Environ. Chem. Eng.* **2017**, *5*, 2459–2468, doi:10.1016/j.jece.2017.04.037.

54. Montañez, J.P.; Heredia, C.L.; Sham, E.L.; Farfán Torres, E.M. Photodegradation of herbicide Metsulfuron-methyl with TiO2 supported on magnetite particles coated with SiO2. *J. Environ. Chem. Eng.* **2018**, *6*, 7402–7410, doi:10.1016/j.jece.2018.07.006.

55. Chakraborty, R.; Asthana, A.; Singh, A.K. Jo ur l P re of. *J. Mol. Liq.* **2020**, 113475, doi:10.1016/j.molliq.2020.113475.

56. Du, T.; Zhou, L.F.; Zhang, Q.; Liu, L.Y.; Li, G.; Luo, W. Bin; Liu, H.K. Mesoporous structured aluminaosilicate with excellent adsorption performances for water purification. *Sustain. Mater. Technol.* **2018**, *18*, e00080, doi:10.1016/j.susmat.2018.e00080.

57. Wen, T.; Wang, J.; Li, X.; Huang, S.; Chen, Z.; Wang, S.; Hayat, T.; Alsaedi, A.; Wang, X. Production of a generic magnetic Fe3O4 nanoparticles decorated tea waste composites for highly efficient sorption of Cu(II) and Zn(II). *J. Environ. Chem. Eng.* **2017**, *5*, 3656–3666, doi:10.1016/j.jece.2017.07.022.

58. Singh, K.K.; Senapati, K.K.; Sarma, K.C. Synthesis of superparamagnetic Fe3O4 nanoparticles coated with green tea polyphenols and their use for removal of dye pollutant from aqueous solution. *J. Environ. Chem. Eng.* **2017**, *5*, 2214–2221, doi:10.1016/j.jece.2017.04.022.

59. Ou, J.; Mei, M.; Xu, X. Magnetic adsorbent constructed from the loading of amino functionalized Fe3O4 on coordination complex modified polyoxometalates nanoparticle and its tetracycline adsorption removal property study. *J. Solid State Chem.* **2016**, *238*, 182–188, doi:10.1016/j.jssc.2016.03.021.

60. Atta, A.M. Antimicrobial Activity of Hybrids Terpolymers Based on Magnetite Hydrogel Nanocomposites. **2019**.

61. Xia, Q.H.; Ma, Y.J.; Wang, J.W. Biosynthesis of Silver Nanoparticles Using Taxus yunnanensis Callus and Their Antibacterial Activity and Cytotoxicity in Human Cancer Cells. **2016**, doi:10.3390/nano6090160.

62. Yasin, Y.S.; Ibrahem, E.J. Antibacterial Activity of Ethanolic Extract of Roots of the Blessed Thistle (Cnicus Benedictus L.). *Cihan Univ. Sci. J.* **2017**, *2017*, 298–310, doi:10.24086/cuesj.si.2017.n2a27.